Removal of the Solar Component in AVHRR 3.7-μm Radiances for the Retrieval of Cirrus Cloud Parameters

N. X. RAO, S. C. OU, AND K. N. LIOU

Department of Meteorology/CARSS, University of Utah, Salt Lake City, Utah

ABSTRACT

A numerical scheme has been developed to remove the solar component in the Advanced Very High Resolution Radiometer (AVHRR) 3.7-μm channel for the retrieval of cirrus parameters during daytime. This method uses a number of prescribed threshold values for AVHRR channels 1 (0.63 μm), 2 (0.8 μm), 3 (3.7 μm), 4 (10.9 μm), and 5 (12 μm) to separate clear and cloudy pixels. A look-up table relating channels 1 and 3 solar reflectances is subsequently constructed based on the prescribed mean effective ice crystal sizes and satellite geometric parameters. An adding–doubling radiative transfer program has been used to generate numerical values in the construction of the look-up table. Removal of the channel 3 solar component is accomplished by using the look-up table and the measured channel 1 reflectance. The cloud retrieval scheme described in Ou et al. has been modified in connection with the removal program. The authors have applied the removal–retrieval scheme to the AVHRR global area coverage daytime data, collected during the First ISCCP (International Satellite Cloud Climatology Project) Regional Experiment cirrus intensive field observation (FIRE IFO) at 2100 UTC 28 October 1986 over the Wisconsin area. Distributions of the retrieved cloud heights and optical depths are comparable to those determined from Geostationary Operational Environmental Satellite visible and IR channels data reported by Minnis et al. Moreover, verifications of the retrieved cirrus temperature and height against lidar data have been carried out using results reported from three FIRE IFO stations. The retrieved cloud heights are within 0.5 km of the measured lidar values.

1. Introduction

Cirrus clouds are global in nature and primarily exist in the upper troposphere and lower stratosphere. These clouds are composed almost entirely of ice crystals. Cirrus clouds play a key role in the global energy balance through latent heat and radiative energy exchanges. Information on cirrus cloud parameters is critically important to the development of cirrus forecast models, the upgrading of real-time global cloud analysis, and the investigation of cloud feedbacks in the global climate change (Liou 1986).

Inference of the microphysical and optical properties of cirrus clouds using satellite or aircraft data has been reported by a number of researchers. Wielicki et al. (1990) used the Landsat 0.83-, 1.65-, and 2.21-μm channel reflectances and phase functions for ice crystals to infer cirrus cloud particle sizes, assuming that single scattering dominates the radiative transfer within cirrus clouds. Liou et al. (1990) developed a physical retrieval method to infer the temperature and optical depth of tropical cirrus anvils using the data of the dual-channel (6.5 and 10.5 μm), downward-viewing, narrow-field-of-view radiometers on board the National Aeronau-

tical and Space Administration's ER-2. Minnis et al. (1993a,b) developed a technique based on the radiative transfer theory and parameterizations to retrieve cirrus optical depth and height using the Geostationary Operational Environmental Satellite (GOES) 0.65- and 11.5-μm channel radiances. Ou et al. (1993) presented a physical retrieval scheme using the Advanced Very High Resolution Radiometer (AVHRR) 3.7- and 10.9-μm channels for the inference of nighttime cirrus cloud parameters, including cloud temperature, optical depth, emissivity, and mean effective ice crystal size based on the theory of radiative transfer and parameterizations. This retrieval scheme has been applied to the nighttime AVHRR satellite data collected at 0930 UTC 28 October 1986 over the region of the First ISCCP (International Satellite Cloud Climatology Project) Regional Experiment (FIRE) cirrus intensive field observation (IFO). The retrieved cirrus height and mean effective ice crystal size compare reasonably well with ground-based lidar and aircraft measurements.

During daytime, the 3.7-μm channel radiance contains both solar reflection and thermal emission. To apply the retrieval scheme to the daytime satellite data, the 3.7-μm channel solar component must be quantified and removed. The problem of removing the 3.7-μm solar reflection (referred to as "sol") and thermal infrared emission (referred to as "IR") component for remote sensing applications has been investigated by

Corresponding author address: Szu-Cheng Ou, Dept. of Meteorology/CARSS, University of Utah, 809 William C. Browning Bldg., Salt Lake City, UT 84112.

several researchers in the past. Arking and Childs (1985) included the solar component of the 3.7-μm channel in the formulation of a general retrieval program for cloud parameters. Kleespies (1993) proposed a dual-observation method to remove the thermal infrared component in the 3.7-μm channel radiances for inferring the particle sizes of opaque marine stratiform clouds. In this paper, we describe a method to remove the solar component in the AVHRR 3.7-μm channel radiance for the retrieval of cirrus cloud parameters during daytime. This method involves various threshold values for AVHRR channels 1 (0.63 μm), 2 (0.8 μm), 3 (3.7 μm), 4 (10.9 μm), and 5 (12 μm), which are prescribed to separate clear and cloudy pixels. A look-up table relating the channel 1 reflectance to the channel 3 solar reflectance is subsequently constructed. This table is based on the effective surface albedos, selected ice crystal sizes, and a set of sun–satellite geometric parameters. A comprehensive adding–doubling radiative transfer program is used to generate numerical values in the look-up table. Removal of the channel 3 solar component is accomplished by using the look-up table and the measured channel 1 reflectance. For retrieval of cloud parameters during daytime, the scheme described in Ou et al. (1993) is modified in connection with the removal program. Section 2 describes the clear–cloud detection scheme and the removal–retrieval procedures. Section 3 presents the results of sensitivity studies and discusses the effects of various possible error sources on the accuracy of removal–retrieval results. In section 4 we demonstrate the applicability of the retrieval algorithm to satellite data. Finally, conclusions are given in section 5.

2. Removal–retrieval scheme

a. Detection of clear and cloudy pixels

The clear–cloud detection scheme is based on several criteria described in Saunders and Kriebel (1988). Figure 1 presents a schematic flowchart of the detection scheme for identifying clear pixels during daytime. The first criterion involves the use of the channel 4 brightness temperature T_4. For a clear pixel, T_4 must be greater than a defined threshold temperature T_{4C}. We may use the map of T_4 over the clear portion of the data domain to derive a mean clear brightness temperature $\bar{T}_4$. The T_{4C} is empirically set as $\bar{T}_4 - 2$ K. Pixels that satisfy the first criterion subsequently undergo the second test, which requires that the channel 1 reflectance r_1 be smaller than a threshold value r_{1C} (i.e., $r_1 < r_{1C}$). The threshold r_{1C} is determined based on the identification of peaks corresponding to cloudy and clear conditions in the histogram of r_1.

Clouds generally have high reflectances, whereas most types of ground and sea surfaces (except snow and ice) have low reflectances at the visible wavelengths. Using this property, a visible threshold may be set up to differentiate between cloudy and clear re-
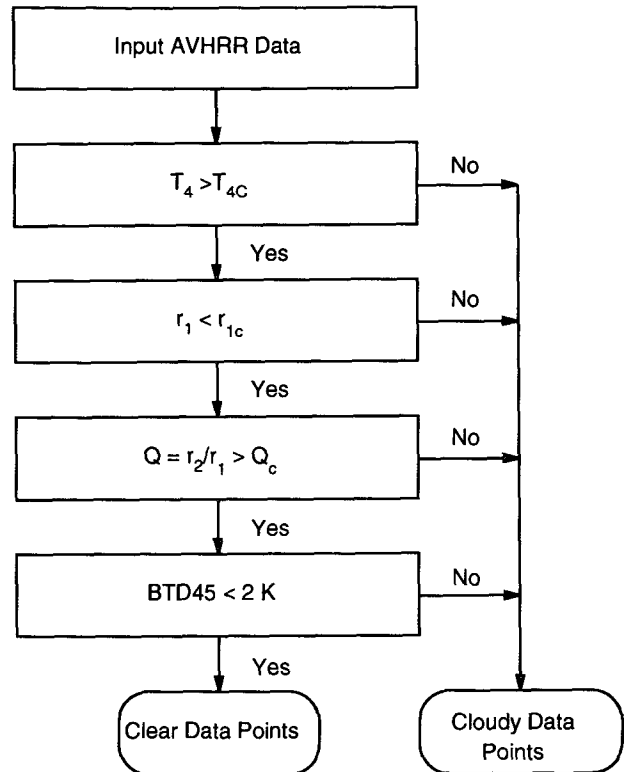

FIG. 1. Flowchart for the daytime clear–cloud detection scheme.

flectances. Because the clear reflectance varies with the surface type, the visible threshold is a function of surface characteristics. The third criterion uses the ratio of channel 2 (0.8 μm) to channel 1 (0.63 μm) reflectances ($Q = r_2/r_1$). This ratio has a unique feature with respect to surface types. For clouds, Q is closer to 1 because the cloud reflectances for these two wavelengths are about the same. Over water surfaces, $Q < 1$ because the reflectance of the 0.63-μm wavelength is more pronounced. Over land with vegetation, $Q \gg 1$ because the reflectance at the 0.8-μm wavelength is much larger than that at the 0.63-μm wavelength. We define a threshold value Q_c such that a pixel is clear if $Q > Q_c$. We have set a uniform value of 1.6 (corresponding to land). This threshold value is applied to all the present retrieval analyses, because most of the area within the retrieval domains are over land. The only significant water surfaces involved are over the Great Lakes region. However, the display of channel 4 brightness temperatures shows that this area is mostly cloudy. Pixels over that area are identified as cloudy by other criteria (see section 4c). Finally, the fourth criterion uses the difference between channel 4 and channel 5 brightness temperatures, which must be less than a threshold value δ ($\sim$2 K). If a pixel satisfies all four criteria, it is identified as clear. Otherwise, it is classified as cloudy. These criteria are complementary to each other. For example, low-cloud pixels are iden-

tified as cloudy because their channel 1 reflectances are higher than the threshold (criterion 2), even though their brightness temperature difference between channels 4 and 5 is smaller than 2 K (criterion 4). Also, pixels associated with thin cirrus are identified as cloudy as long as their channel 4 brightness temperatures are lower than the threshold value (criterion 1), even though their channel 1 reflectances and brightness temperature differences are lower than threshold values.

b. Removal of 3.7-μm solar component

Let the angle of the incident solar radiation is θ_0, while the satellite viewing angle is θ. The relative azimuthal angle $\Delta\phi$ is defined as the angle between the horizontal projection planes of the sun and the satellite. We define μ_0 and μ to be the cosines of the solar and satellite zenith angles, respectively. Moreover, let the channels 1 and 3 solar reflectances in the direction of (μ, $\Delta\phi$) for cirrus cloudy conditions be $r_1(\mu_0, \mu, \Delta\phi)$ and $r_3(\mu_0, \mu, \Delta\phi)$, respectively, which can be evaluated from the following parametric equation (Liou 1980, p. 216; Arking and Childs 1985):

$$r_i(\mu_0, \mu, \Delta\phi) = r_i^*(\mu_0, \mu, \Delta\phi) + \frac{\gamma_i(\mu)\gamma_i(\mu_0)r_{ai}}{1 - r_{ai}\bar{r}_i},$$

$$i = 1, 3, \quad (1)$$

where $r_i^*(\mu_0, \mu, \Delta\phi)$ are the solar reflectances due to cloud layer only, $\bar{r}_i$ are the albedos of the cloud layer, and r_{ai} are the effective surface albedos that take into account the Rayleigh scattering effects in the visible spectral region and the water vapor absorption effects in the near-IR region. Moreover, $\gamma_i(\mu)$ and $\gamma_i(\mu_0)$ are the total directional transmittances in the direction of (μ, $\Delta\phi$) and (μ_0, 0), respectively. These transmittances are composed of direct and diffuse transmittances of the incoming radiation as follows:

$$\gamma_i(\mu) = e^{-\tau_i/\mu} + t_i(\mu), \quad (2)$$

where τ_i are the optical depths for channels 1 and 3, and t_i are given by

$$t_i(\mu) = \frac{1}{\pi}\int_0^{2\pi}\int_0^1 t_i^*(\mu', \mu, \Delta\phi)\mu'd\mu'd(\Delta\phi), \quad (3)$$

where $t_i^*(\mu', \mu, \Delta\phi)$ are the downward transmitted diffuse radiances in the direction μ for channels 1 and 3, and F_{0i} are the respective incident solar irradiances. The albedo of clouds can be obtained from the following (Liou 1980, p. 202):

$$\bar{r}_i = 2\int_0^1 r_i'(\mu)\mu d\mu, \quad (4)$$

where $r_i'(\mu)$ are defined similarly to Eq. (3). Finally, the second term in Eq. (1) represents the fraction of incoming solar radiation that is reflected to the satellite

due to multiple reflections between the surface and the cloud base.

We develop a look-up table relating $r_1(\mu_0, \mu, \Delta\phi)$ and $r_3(\mu_0, \mu, \Delta\phi)$ based on Eq. (1) for different satellite viewing geometries and cirrus cloud optical and microphysical properties. In Fig. 2, the procedures for the construction of such a look-up table for removing the 3.7-μm solar radiance are outlined. We first estimate the mean channel 1 effective surface albedo r_{a1} using satellite data. Once clear pixels are identified via the preceding detection scheme, the angular dependent channel 1 solar reflectance $r_1(\mu_0, \mu, \Delta\phi)$ for each clear pixel is computed from the satellite data $\tilde{r}_1(\mu, \Delta\phi)$, which has been normalized with respect to the incident solar radiation in the zenith direction as follows:

$$r_1(\mu_0, \mu, \Delta\phi) = \frac{\tilde{r}_1(\mu, \Delta\phi)}{\mu_0}. \quad (5)$$

Subsequently, we construct a one-dimensional histogram of $r_1(\mu_0, \mu, \Delta\phi)$ for all clear pixels and directly
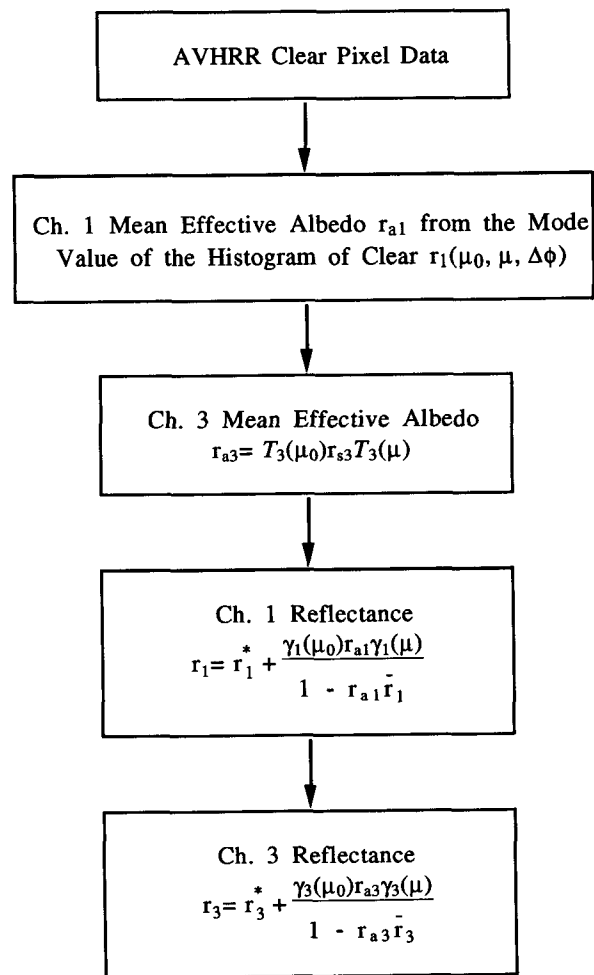

FIG. 2. Flowchart for the construction of a look-up table involving the correlation between channel 1 and channel 3 solar reflectances.

estimate r_{a1} from the peak value of the histogram. This procedure will yield reasonable values of r_{a1} because the channel 1 clear radiance contains the effects of Rayleigh scattering.

The preceding procedure is not applicable to evaluating the channel 3 effective surface albedo r_{a3} since the channel 3 clear radiance contains both solar and thermal infrared components. The magnitude of the thermal infrared component is generally unknown. To estimate r_{a3}, we use the following formula based on the radiative transfer principle:

$$r_{a3} = T_3(\mu_0)r_{s3}T_3(\mu), \qquad (6)$$

where $T_3(\mu)$ is the total atmospheric transmittance in the direction of μ, and r_{s3} is the channel 3 surface albedo. The three terms in Eq. (6) represent downward atmospheric transmission, surface reflection, and upward atmospheric transmission of solar radiation, respectively. Since the effects of Rayleigh scattering on the transfer of the 3.7-μm wavelength are relatively weak, multiple reflections between the surface and the Rayleigh layer are neglected in Eq. (6). Based on calculations using the LOWTRAN program and the U.S. standard atmosphere profile (Air Force Geophysics Laboratory 1985), the atmospheric transmittance between 3.6 and 4.0 μm is on the order of 0.85–0.90.

The exact value of r_{s3} is also unknown. However, from laboratory measurements (Sutherland 1986) the 3.7-μm surface emissivity varies between 0.8 and 1.0 for several types of natural soil and vegetation. Thus, the surface albedo r_{s3} has a value between 0.0 and 0.2 based on Kirchhoff's law. Bunting and Hardy (1974) presented an average r_{s3} value of 0.15 for the snow-free land. Allen et al. (1990) reported that for snow, r_{s3} depends on the snow grain size and varies between 0.005 and 0.025. Based on the preceding values, r_{s3} is set as 0.1 in the present removal scheme. Once the effective surface albedos for channels 1 and 3 are determined, we then proceed to compute the solar reflectances of the two channels following Eq. (1). For this purpose, we compute the single-scattering properties based on the measured ice crystal size distributions. Details of this step are described in the following.

We have analyzed six composite ice crystal size distributions that were obtained from the data presented by Heymsfield and Platt (1984), Takano and Liou (1989a), and the FIRE IFO microphysical data. They are denoted as cold Ci, −60°C, Cs, FIRE IFO 1 Nov, FIRE IFO 2 Nov, and Ci uncinus. We first define a mean effective width (or size) to represent ice crystal size distribution in the form

$$D_e = \frac{\int_{L_{min}}^{L_{max}} D^2 Ln(L)dL}{\int_{L_{min}}^{L_{max}} DLn(L)dL}, \qquad (7)$$

where D and L denote the width and the maximum dimension of a nonspherical ice crystal, respectively, and $n(L)$ is the size distribution in terms of L. The rationale for defining D_e to represent ice crystal size distribution is that the scattering of light is related to the geometric cross section, which is proportional to LD. Light scattering and absorption programs developed by Takano and Liou (1989a) for hexagonal ice crystals have been used to compute single-scattering properties as functions of D_e. To compute D_e, we use the empirical relationship of L and D based on laboratory data (Auer and Veal 1970):

$$D = aL^b, \qquad (8)$$

where a and b are empirical coefficients. Each size distribution is discretized into five intervals, and D_e is computed by summation of the integrands in Eq. (7). The single-scattering albedos $\bar{\omega}$, phase functions, and extinction coefficients $\bar{\beta}_e$ for given ice crystal size distributions are computed from the following equations:

$$\bar{\omega} = \frac{\int_{L_{min}}^{L_{max}} \beta_s n(L)dL}{\int_{L_{min}}^{L_{max}} \beta_e n(L)dL}, \qquad (9)$$

$$\bar{P}(\Theta) = \frac{\int_{L_{min}}^{L_{max}} P(\Theta)\beta_s n(L)dL}{\int_{L_{min}}^{L_{max}} \beta_s n(L)dL}, \qquad (10)$$

$$\bar{\beta}_e = \int_{L_{min}}^{L_{max}} \beta_e n(L)dL, \qquad (11)$$

where β_s and β_e are the scattering and extinction cross sections, respectively, and $P(\Theta)$ is the phase function as a function of the scattering angle Θ. Table 1 lists the values of D_e, $\bar{\omega}$, $\bar{g}$, and $\bar{\beta}_e$ for six measured ice crystal size distributions, whose $\bar{g}$ is the asymmetry factor associated with the phase function. For 0.63 μm, $\bar{\omega}$ is very close to 1 for all D_e's, while for 3.7 μm, $\bar{\omega}$ decreases from 0.79 for the smallest D_e to 0.59 for the largest D_e. Moreover, $\bar{g}$ for both wavelengths increases with D_e. The implication of these behaviors in the removal of the 3.7-μm solar component will be discussed in the following.

The single-scattering parameters for hexagonal ice columns and plates (Takano and Liou 1989a) are used in the adding–doubling radiative transfer program developed by Takano and Liou (1989b) to compute $r_i^*(\mu_0, \mu, \Delta\phi)$, $\gamma_i(\mu)$, $\gamma_i(\mu_0)$, and $\bar{r}_i$. This ice crystal model is the best we have so far. The effects of ice crystal shapes on the single-scattering properties as they pertain to remote sensing applications is a subject requiring further investigations. In the computations, we use 10 optical depths ranging from 0.125 to 64. Figure 3 shows an example of the relationship between the

reflectances r_3 and r_1 for the six ice crystal size distributions and the prescribed viewing geometry. Numbers in parentheses are D_e values. Values of effective surface albedos for channels 1 and 3, r_{a1} and r_{a3}, are specified to be 0.12 and 0.046, respectively. It is noted that radiances of both channels converge to the values of r_{a1} and r_{a3} for thin cirrus. Reflectance r_3 reaches asymptotic values for $r_1 > 0.4$ due to saturated absorption by clouds with large optical depth. Moreover, this asymptotic value decreases with increasing D_e, because $\bar{\omega}$ decreases with increasing D_e and $\bar{g}$ increases with increasing D_e. The preceding analyses have the following implications. First, the removal of 3.7-μm solar component depends on the values of r_{a1} and r_{a3} for thin cirrus clouds. However, this dependence becomes less significant for $r_1 > 0.4$. Thus, it is important to specify the values of r_{a1} and r_{a3} as accurately as possible if thin cirrus clouds are involved. We may improve the initial guess for r_{a3} by determining r_{s3} from the information of surface land type. Second, for $r_1 > 0.4$, r_3 depends on D_e only. Thus, it is possible to estimate r_3, T_c, and D_e directly from channels 1, 3, and 4 radiances for thick cirrus. Finally, for $D_e > 100$ μm, r_3 is independent of D_e as it approaches a minimum value of approximately 0.02 for the present set of geometric parameters.

Once the look-up correlation table is established, the solar component in the 3.7-μm radiances is removed with the aid of the 0.63-μm reflectance and a trial mean effective ice crystal size. After this removal, the remaining thermal infrared radiance of 3.7 μm coupled with the 10.9-μm radiance is used to perform retrieval using the program developed by Ou et al. (1993) to obtain the cirrus cloud temperature, mean effective ice crystal size (from cloud temperature), and emissivity. A brief overview of the retrieval methodology is given in the next section.

c. Retrieval of cirrus cloud parameters

The retrieval methodology follows the principles of the dual thermal infrared channel technique presented in Liou et al. (1990) and Ou et al. (1993). The retrieval of cirrus cloud parameters is based on the numerical
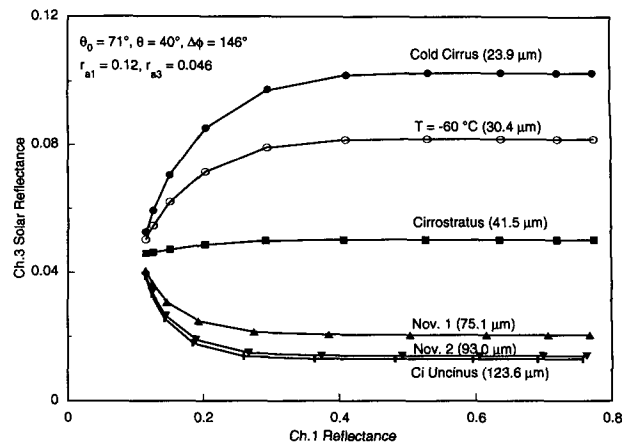

FIG. 3. Correlations between the channel 3 solar reflectance r_3 and channel 1 reflectance r_1 for six measured ice crystal size distributions.

solution of the following set of nonlinear algebraic equations derived from the theory of radiative transfer and parameterizations:

$$R_i = R_{ai}(1 - \epsilon_i) + \epsilon_i B_i(T_c), \qquad (12)$$

$$\epsilon_i = 1 - \exp(-k_i \tau), \quad i = 3, 4, \qquad (13)$$

$$B_3(T_c) = \sum_{n=0}^{3} a_n[B_4(T_c)]^n, \qquad (14)$$

where R_i is the upwelling thermal infrared radiance at the top of the atmosphere for channels 3 and 4 over cirrus clouds, R_{ai} is the corresponding thermal infrared radiance reaching the cloud base for the two channels, ϵ_i is the cloud emissivity, T_c is the equivalent radiating cirrus temperature, $B_i(T_c)$ is the Planck intensity at T_c, τ is the visible optical depth (simply referred to as optical depth), and k_i is the adjustment factor to account for scattering and wavelength difference, referred to as the effective extinction coefficients. Polynomial form is used to relate $B_3(T_c)$ and $B_4(T_c)$ in Eq. (14). Because both $B_3(T_c)$ and $B_4(T_c)$ are smooth functions of T_c, polynomial fitting of these values gives very small errors (<1%). The values of polynomial coefficients

TABLE 1. Single-scattering properties for six ice crystal size distributions, where D_e is the mean effective ice crystal size, $\bar{\beta}_e$ is the extinction coefficient, $\bar{\omega}$ is the single-scattering albedo, and $\bar{g}$ is the asymmetry factor.

Cirrus type	D_e (μm)	0.63 μm			3.7 μm		
		$\bar{\beta}_e$ (km^{-1})	$\bar{\omega}$	$\bar{g}$	$\bar{\beta}_e$ (km^{-1})	$\bar{\omega}$	$\bar{g}$
Cold Ci	23.9	0.16623	0.999997	0.77125	0.16620	0.79116	0.80632
−60°C	30.4	0.07596	0.999996	0.77565	0.07596	0.76369	0.82345
Cs	41.5	0.38650	0.999995	0.78367	0.38653	0.71298	0.85821
FIRE IFO 1 Nov	75.1	0.20209	0.999990	0.81659	0.20210	0.63263	0.91367
FIRE IFO 2 Nov	93.0	0.44736	0.999988	0.83065	0.44736	0.60636	0.93177
Ci uncinus	123.6	2.60580	0.999984	0.83966	2.60580	0.58885	0.93561

TABLE 2. Values of the effective extinction ratio k_4/k_3 as a function of the mean effective size D_e. Values of D_e are computed from a number of measured ice crystal size distributions.

D_e (μm)	k_4/k_3
23.9	2.725
30.4	2.364
41.5	1.792
47.5	1.908
57.9	1.705
64.1	1.585
75.1	1.347
93.0	1.231
104.1	1.242
106.7	1.224
110.4	1.212
123.6	1.182

are $a_0 = 2.6327 \times 10^{-4}$, $a_1 = -1.063 \times 10^{-4}$, $a_2 = 8.2976 \times 10^{-6}$, and $a_3 = 3.7311 \times 10^{-7}$.

The solution involves the effective extinction ratio for the two channels k_4/k_3, which is dependent on D_e. To investigate the dependence of the effective extinction ratio on D_e, we have used the light scattering and radiative transfer program developed by Takano and Liou (1989a,b) to compute k_4/k_3 as a function of D_e. Table 2 shows the dependence k_4/k_3 on D_e based on 12 measured size distributions (Ou et al. 1993). The value of k_4/k_3 increases as D_e becomes smaller, implying that more scattering is associated with the 3.7-μm wavelength than 10.9 μm. Thus, it is necessary to know D_e in order to compute k_4/k_3. In the dual-channel technique (6.5 μm and 10.5 μm) developed by Liou et al. (1990), information of the ice crystal size is not required because the dependence of the emissivity on the size is negligible in these two wavelengths. A second-degree polynomial least-squares fitting for this ratio in terms of $1/D_e$ has been developed:

$$\frac{k_4}{k_3} = \sum_{n=0}^{2} b_n D_e^{-n},\tag{15}$$

where $b_0 = 0.722$, $b_1 = 55.08$, and $b_2 = -174.12$.

Based on a large number of cirrus microphysical data collected by optical probes during flights over midlatitudes, Heymsfield and Platt (1984) have developed a

functional form for the measured ice crystal size distribution using a general power form as follows:

$$n(L) = \begin{cases} A_1 L^{B_1}(\text{IWC}), & L \leqslant L_0, \\ A_2 L^{B_2}(\text{IWC}), & L > L_0, \end{cases}\tag{16}$$

where $L_0 = (A_2/A_1)^{1/(B_1-B_2)}$; IWC is the ice water content, which can be parameterized as a function of temperature (Liou 1992); and $A_{1,2}$ and $B_{1,2}$ are temperature-dependent coefficients determined from the measured data. Table 3 lists the values of constants in Eq. (16). According to this parameterization, D_e is a function of temperature. We perform a least-squares polynomial fitting to relate D_e to cloud temperature T_c in the form

$$D_e = \sum_{n=0}^{3} c_n(T_c - 273)^n,\tag{17}$$

where $c_0 = 326.3$, $c_1 = 12.42$, $c_2 = 0.197$, and $c_3 = 0.0012$. From this equation, D_e increases with increasing T_c, which is consistent with recent aircraft microphysics measurements reported by Heymsfield et al. (1990).

To solve Eqs. (12)–(14), the upwelling radiances reaching the cloud base R_{ai} must be given. They are determined by using the radiances of clear pixels, because very little water vapor is present above cirrus clouds. It follows that if we can identify the clear pixels, R_{ai} may be determined by a statistical method. We may select a scene and use the data within this scene to construct a two-dimensional histogram in the domain of R_3 and R_4. The radiances corresponding to the peak of the frequency distribution are assigned as the mean clear radiances. The area of the scene should be large enough to contain a statistically significant amount of pixels. At the same time, this area should also be sufficiently small to guarantee the homogeneity of the surface temperature and water vapor distributions within the scene. Ou et al. (1993) used the FIRE IFO data and two sizes (1° × 1° and 0.5° × 0.5°) to investigate the effects of varying the area size on the retrieval and found that the variability of the clear radiances decreases with decreasing size of the area. However, the mean clear radiances remain unchanged. Both Minnis et al. (1993b) and Chou (1991) used the

TABLE 3. Values of A_1, A_2, B_1, B_2, L_0, and IWC in Eq. (16) as functions of temperature.

Temperature (°C)	A_1	A_2	B_1	B_2	L_0 (μm)	IWC (g m^{-3})
−20 to −25	6.837×10^8	3.304×10^{12}	−2.56	−3.74	977	0.0270
−25 to −30	7.328×10^8	3.068×10^{14}	−2.51	−4.49	691	0.0250
−30 to −35	1.954×10^8	9.063×10^{12}	−2.21	−3.94	498	0.0175
−35 to −40	7.540×10^8	1.329×10^{14}	−2.29	−4.37	333	0.0126
−40 to −45	2.163×10^{12}	—	−3.23	—	—	0.0034
−45 to −50	1.117×10^{11}	—	−3.15	—	—	0.0025
−50 to −55	1.778×10^{11}	—	−3.83	—	—	0.0018
−55 to −60	2.800×10^{11}	—	−3.85	—	—	0.0009

ISCCP grid ($2.5° \times 2.5°$) for the determination of clear radiances.

d. Removal–retrieval scheme

Both the removal and retrieval programs are dependent on the ice crystal size distribution represented by the mean effective size D_e. The mean effective sizes are computed on a pixel-by-pixel basis. They are determined from the retrieved cloud temperature based on the relationship between the mean effective size and cloud temperature [Eq. (17)] and not selected out of the six measured size distributions presented in Fig. 3. A value of $D_e^{(0)}$ is prescribed initially. This value is usually the largest possible value of D_e, which corresponds to the minimum amount of solar radiances to be removed. Using satellite-derived r_{a1} and prescribed r_{s3}, a look-up table for r_3 versus r_1 is constructed according to the procedures described in section 2b. The solar reflectance r_3 is then obtained from the measured 0.63-μm reflectance and the look-up table. Let the reflected radiance of channel 3 be R_{3sol}. Thus,

$$R_{3sol} = \mu_0 F_{03} r_3, \qquad (18)$$

where F_{03} is the incident solar irradiance, which is obtained from Thekaekara (1974), and r_3 is the solar reflectance for the 3.7-μm channel. Let the thermal infrared component of channel 3 be R_{3ir}. The initial value for R_{3ir} is obtained from the following:

$$R_{3ir}^{(0)} = R_3 - R_{3sol}^{(0)}. \qquad (19)$$

Both $R_{3ir}^{(0)}$ and R_4 [Eq. (12)] are used in the cirrus retrieval program. The same $D_e^{(0)}$ as in the removal scheme is used to specify k_4/k_3 according to Eq. (15). A new cirrus cloud temperature $T_c^{(0)}$ is then obtained. From $T_c^{(0)}$ we may compute an intermediate value for $\tilde{D}_e^{(1)}$ using Eq. (17). Because we have removed the minimum amount of the 3.7-μm solar component, the thermal infrared component $R_{3ir}^{(0)}$ will be overestimated based on Eq. (19). From Eqs. (12) and (17), $T_c^{(0)}$ and $\tilde{D}_e^{(1)}$ will be underestimated. Thus, the difference $|\tilde{D}_e^{(1)} - \tilde{D}_e^{(0)}|$ would be substantial. If we apply $\tilde{D}_e^{(1)}$ to the removal–retrieval scheme, numerical instability may occur. To avoid this, a new suppressed value of $D_e^{(1)}$ is computed as follows:

$$D_e^{(1)} = \alpha \tilde{D}_e^{(1)} + (1 - \alpha) D_e^{(0)}. \qquad (20)$$

The suppression factor α is on the order of 0.005. The use of such a small value for α maintains the stability in numerical iterations. Using the new value for $D_e^{(1)}$, we repeat the above removal–retrieval procedures to obtain $D_e^{(2)}$. The iteration process is carried out until $D_e^{(n)}$ satisfies the following convergence criterion:

$$\frac{|D_e^{(n)} - D_e^{(n-1)}|}{D_e^{(n-1)}} < 1.0 \times 10^{-4}. \qquad (21)$$

3. Sensitivity studies and error analyses

Sensitivity studies have been performed using the midlatitude summer atmospheric profile. First, we must generate simulated thermal infrared and solar clear and cloudy radiances. Spectral transmittances for the 3.7- and 10.9-μm wavelengths have been computed by using the program developed by Weinreb and Hill (1980), in which the instrument filter function is accounted for. The simulated upwelling IR radiances for clear sky are computed using the solution of the basic radiative transfer equation in the forms

$$R_{a3ir} = B_3(T_s) T_3(p_s) + \int_0^{p_s} B_3(T) \frac{\partial T_3(p)}{\partial p} \, dp, \quad (22a)$$

$$R_{a4} = B_4(T_s) T_4(p_s) + \int_0^{p_s} B_4(T) \frac{\partial T_4(p)}{\partial p} \, dp, \quad (22b)$$

where p_s and T_s are the surface pressure and temperature, respectively, and $T_i(p)$ are the atmospheric transmittances at pressure level p. In the simulations, cloud-base heights are prescribed at 7, 9, and 11 km. The cloud temperatures and mean ice crystal sizes can be determined from the temperature profile. For each cloud-base height, calculations are carried out for 10 optical depths (0.125, 0.25, 0.5, 1.0, 2.0, 4.0, 8.0, 16.0, 32.0, 64.0). Emissivity values are obtained from Eq. (13). The upwelling thermal infrared cloudy radiances are then computed from Eq. (12).

To compute the channel 3 solar radiance for clear and cloudy skies, we first set the effective surface albedos for channels 1 and 3 to be 0.12 and 0.1, respectively. The geometric parameters used are solar zenith angle, $\theta_0 = 71°$; satellite zenith angle, $\theta = 40°$; and relative azimuthal angle, $\Delta \phi = 146°$. This set is based on the geometric parameters involving the FIRE IFO data. The clear solar radiance for channel 3 is computed as follows:

$$R_{a3sol} = \mu_0 F_{03} r_{a3}, \qquad (23)$$

while the cloudy solar radiance for channel 3 is computed from Eq. (18). It follows that the simulated channel 3 radiances for both cloudy and clear atmospheres are given by

$$R_3 = R_{3ir} + R_{3sol}, \qquad (24)$$

$$R_{a3} = R_{a3ir} + R_{a3sol}. \qquad (25)$$

Figures 4a and 4b show the distributions of R_{3ir} and R_3 ($= R_{3sol} + R_{3ir}$) versus R_4, respectively, for the three cloud heights and 10 optical depths. In each plot, the Planck intensity curve is included as a reference. The curves of constant cloud height are all above the Planck intensity curve. The uppermost point where all the curves converge represents clear radiances. The lowest point for each curve corresponds to the highest optical depth. The curvature of the curves in Fig. 4b is due to the variation in R_{3sol}. By comparing Figs. 4a and 4b,
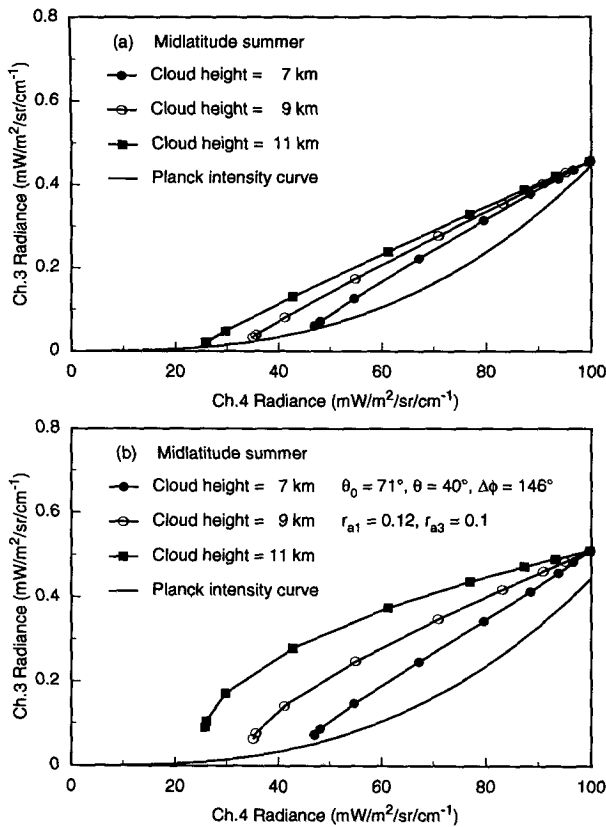
FIG. 4. (a) Distribution of the simulated channel 3 thermal infrared (R_{3ir}) and channel 4 (R_4) radiances for three cloud heights. Also depicted in the figure is the Planck intensity curve. (b) Distribution of the simulated channel 3 solar plus thermal infrared (R_3) and channel 4 (R_4) radiances for the same three cloud heights.

we note that R_3 is larger than R_{3ir} by about 0.05–0.2 mW m^{-2} sr^{-1} cm due to additional solar reflections for the present sun–satellite geometry. This difference will increase as the sun becomes closer to the zenith. Moreover, in Fig. 4a, when the emissivity approaches 1 for the largest optical depth, both R_{3ir} and R_4 approach $B_3(T_c)$ and $B_4(T_c)$, respectively. However, in Fig. 4b, the total channel 3 radiance $R_3 > B_3(T_c)$. The difference between R_3 and $B_3(T_c)$ is mainly due to the size effect on the solar component as well as the atmospheric absorption and surface reflection.

Figure 5 illustrates the ratio of R_{3sol} to R_{3ir} as a function of τ and cloud-base height. Variation in the relative magnitude of R_{3sol} and R_{3ir} can be seen. For the present sun–satellite geometry, this ratio increases with τ. For thin cirrus ($\tau < 1$), R_{3ir} is 10 times larger than R_{3sol} and is almost independent of cloud height. However, for thick cirrus, R_{3sol}/R_{3ir} approach asymptotic values, because R_{3ir} approaches the Planck intensity value at the cirrus cloud temperature. The R_{3sol} also approaches its asymptotic value. Moreover, the radiance ratio increases with the cloud-base height because of the coupling of lower cloud temperatures and smaller ice crys-

tals. The former leads to smaller R_{3ir} values, while the latter produces stronger solar reflection. For the present sun–satellite geometry, Fig. 5 shows that the channel 3 solar component is at least 10% of the total radiance, which cannot be ignored.

In the following, we investigate the effects of uncertainties in the input parameters on the accuracy of the removed solar component. Errors in the 3.7-μm solar component can be due to uncertainties in the mean effective size D_e, as well as the channels 1 and 3 effective surface albedos r_{a1} and r_{a3}.

First, the effects of uncertainties in D_e on the accuracy of the channel 3 solar radiance R_{3sol} are studied. From the three prescribed cloud-base heights of 7, 9, and 11 km, mean D_e values of 136, 81, and 52 μm are obtained. Next, R_{3sol} and the total channel 3 radiance R_3 are computed for each D_e value as well as for a number of optical depths. We assume that r_{a1} and r_{a3} are the exact values and that the value of D_e used in the scheme has a range of uncertainty, $\Delta D_e = \pm 5 \ \mu$m. We then proceed to quantify R_{3sol} by using the lookup table as displayed in Fig. 3. Errors in R_{3sol} will result due to the uncertainty in D_e. Figure 6a shows the maximum percentage errors for $\Delta R_{3sol}/R_{3sol}$ as functions of optical depth. The relative error $\Delta R_{3sol}/R_{3sol}$ increases with the optical depth. For small optical depths, ΔR_{3sol} is small because R_{3sol} is dominated by surface reflection. For thicker clouds, the reflected radiances are dominated by cloud reflection and the effects of ΔD_e become important. Since R_{3sol} approaches an asymptotic value for $R_1 > 0.4$ (Fig. 3) and since the range of ΔD_e is fixed at $\pm 5 \ \mu$m, $\Delta R_{3sol}/R_{3sol}$ also approaches an asymptotic value. The error in $\Delta R_{3sol}/R_{3sol}$ for the 7-km cloud case is smaller than the errors for the 9- and 11-km cloud cases because the former has a D_e larger than 100 μm. Note that R_{3sol} is nearly constant for $D_e > 100 \ \mu$m (Fig. 3). Overall, the maximum error of $\Delta R_{3sol}/R_{3sol}$ is less than 12%.
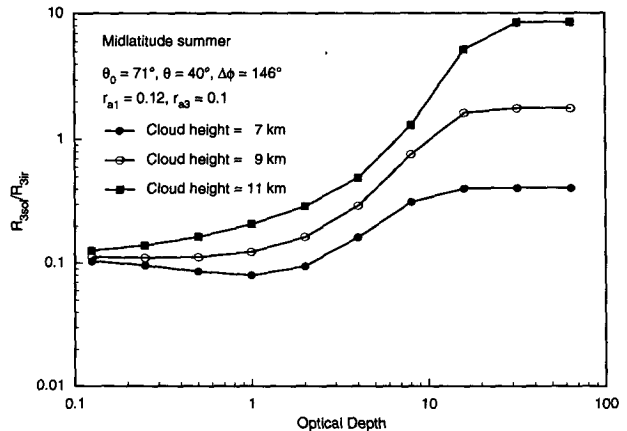

FIG. 5. The ratio of the channel 3 solar (R_{3sol}) to IR (R_{3ir}) components as a function of the optical depth for three cloud heights.
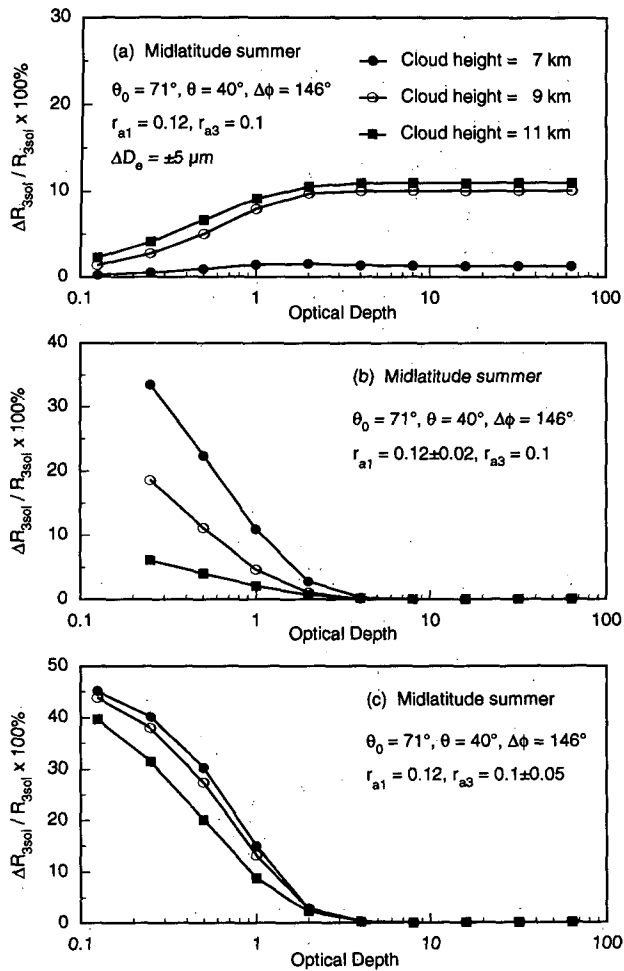
FIG. 6. Maximum percentage errors in the channel 3 solar radiances R_{3sol} produced by the errors in (a) the mean effective size ΔD_e of ± 5 μm, (b) the channel 1 mean effective surface albedo Δr_{a1} of ± 0.02, and (c) the channel 3 mean effective surface albedo Δr_{a3} of ± 0.05.

Next we investigate the effects of uncertainties in r_{a1} on the accuracy of R_{3sol}. We assume that D_e and r_{a3} are both known without errors, but r_{a1} has an uncertainty of ± 0.02. Errors in R_{3sol} will be produced due to the uncertainty in r_{a1}. Figure 6b shows the maximum percentage errors in R_{3sol} as functions of optical depth. In contrast to Fig. 6a, $\Delta R_{3sol}/R_{3sol}$ decreases as the optical depth increases. This decrease occurs because the reflected radiances are essentially controlled by cloud reflection for larger optical depths, so that the changes in the effective surface albedo have little effect. For smaller optical depths, $\Delta R_{3sol}/R_{3sol}$ is larger for the 7-km cloud than for the 9- and 11-km clouds, because R_{3sol} is much smaller for larger D_e's associated with the 7-km cloud. Overall, for optical depths larger than 1, the maximum $\Delta R_{3sol}/R_{3sol}$ is less than 12%.

We also investigate the effects of uncertainties in r_{a3} on the accuracy of R_{3sol}. It is assumed that D_e and r_{a1} values are exact. However, r_{a3} has an uncertainty of

± 0.05, which will result in errors in R_{3sol}. Figure 6c shows the maximum percentage errors in R_{3sol} as functions of optical depth. As in Fig. 6b, $\Delta R_{3sol}/R_{3sol}$ decreases as the optical depth increases. In addition, for smaller optical depths, $\Delta R_{3sol}/R_{3sol}$ is smaller for the 11-km cloud because the value of R_{3sol} is larger for smaller D_e associated with higher clouds. For optical depths larger than 1, the maximum $\Delta R_{3sol}/R_{3sol}$ is less than 15%.

Errors in the retrieved cirrus parameters can be due to instrument noises and the errors in r_{a1} and r_{a3}. To perform error analyses, the probability of the error produced by a particular parameter x (Δx) is assumed to follow the Gaussian distribution in the form

$$p(\Delta x) = \frac{1}{\sigma(2\pi)^{1/2}} \exp\left[-\left(\frac{\Delta x^2}{2\sigma^2}\right)\right], \quad (26)$$

where σ is the standard deviation. The Gaussian distribution differs from random distribution in that the latter would give a uniform probability of error within the prescribed error bounds, while the former would give a decreasing probability of error as the error increases. The Gaussian distribution appears to be more representative of a realistic error distribution than the random distribution. We have used an established software as the Gaussian distribution generator to simulate various error distributions with the following specified standard deviations: for the channel 3 noise, $\sigma = 0.4$ K; for the channel 4 noise, $\sigma = 0.12$ K; for the channel 1 effective surface albedo, $\sigma = 0.02$; and for the channel 3 effective surface albedo, $\sigma = 0.05$. The σ values for channel 3 and channel 4 noises are prescribed based on the values described by Dudhia (1989). The σ value for the channel 1 surface albedo is based on the realistic histogram for channel 1 reflectances. The σ value for the channel 3 mean effective surface albedo is based on the range of laboratory measurements (Sutherland 1986) for 3.7-μm surface reflectances.

To carry out the error analysis, we generate 3000 sets of errors in both instrument noises and the prescribed parameters. Figures 7a–d show, respectively, the root-mean-square (rms) errors for the channel 3 solar component, the cirrus cloud temperature, the mean effective size, and the optical depth as functions of the prescribed optical depth for three cloud-base heights. In all cases, rms errors decrease with increasing optical depths because the effects of the uncertainty in effective surface albedo on cloudy radiances become less as the optical depth increases. Moreover, for thin cirrus clouds, slight perturbations in both radiances due to instrument noises would lead to large errors in the retrieved parameters. For optical depths larger than 8, the percentage error in the optical depth increases (Fig. 7d) because the emissivity approaches 1 and a slight error in it would lead to a large error in the optical depth. For optical depths greater than 0.25, the rms
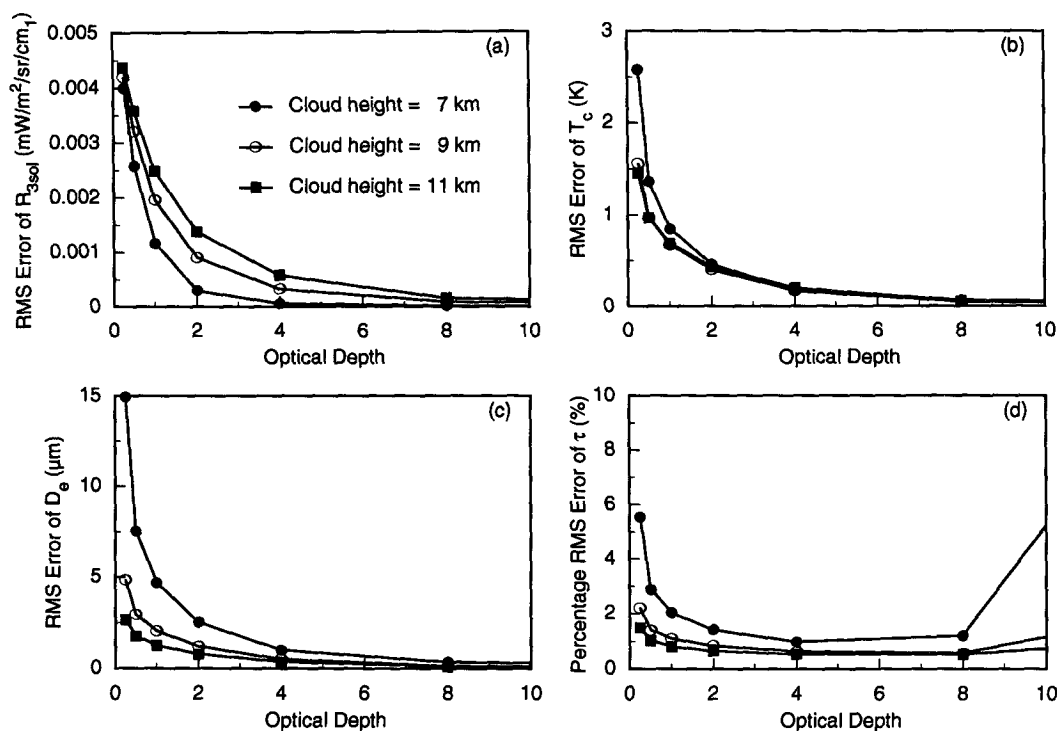
FIG. 7. Root-mean-square errors in (a) the channel 3 solar component, (b) cirrus cloud temperature, (c) mean effective size, and (d) optical depth produced by channel 3 noise ($\sigma = 0.4$ K), channel 4 noise ($\sigma = 0.12$ K), uncertainties in channel 1 surface albedo ($\sigma = 0.02$), and uncertainties in channel 3 surface albedo ($\sigma = 0.05$) as functions of the optical depth.

errors in R_{3sol}, T_c, D_e, and τ are less than 0.0045 mW m^{-2} sr^{-1} cm (or 5%), 2.6 K, 15 μm, and 6%, respectively, indicating that the removal–retrieval scheme is numerically stable and the retrieval accuracy is acceptable. The rms errors in T_c are of the same order of magnitude as the rms differences between the retrieved and lidar derived values (Table 3), (Minnis et al. 1993b). Moreover, the rms errors in D_e are less than the uncertainty in the D_e determined from the aircraft measurements (Heymsfield and Platt 1984).

The retrieval accuracy depends on the cloud height and varies for the retrieved cloud parameters. Errors in R_{3sol} increase with decreasing cloud height. Errors in T_c are virtually independent of cloud height for optical depths greater than 2. However, for optical depths smaller than 2, errors increase with decreasing cloud height. This behavior is related to errors in D_e, which increase with decreasing cloud height as shown in Fig. 7c. In the retrieval scheme, the parameters D_e, k_4/k_3, and T_c and the associated errors are interrelated through Eqs. (15) and (17). Moreover, when the cloud is lower, cloud temperature is higher, while ice crystal size is larger and k_4/k_3 approaches its asymptotic values in the case of lower clouds. A small error in k_4/k_3 would lead to large errors in both D_e and T_c. Finally, in Fig. 7d, errors in the optical depth are shown to increase with decreasing cloud height. This implies that errors

in the related cloud emissivity increase with cloud temperature.

Effects of other uncertainties on the accuracy of the removal–retrieval scheme are discussed in the following. Based on Fig. 3, errors in the channel 1 radiance do not affect significantly the accuracy of the removed solar component for optical depths larger than 1, because the channel 3 radiance is close to the asymptotic value. For optical depths smaller than 1, errors of the removed solar component depend on the effective surface albedo for both channels and the ice crystal sizes. The inhomogeneity of cirrus clouds would have an important effect on their radiative properties. However, it is not feasible to retrieve the detailed structure of clouds using the infrared methodology. The retrieval results would represent the averaged cloud characteristics over the AVHRR pixels. It appears to us that the effects of ice crystal shape and cloud inhomogeneity on the radiative properties of clouds will require considerable research before their impacts on satellite remote sensing can be understood. Finally, regarding the effects of errors in the polynomial fitting of k_4/k_3 versus D_e, we have shown that the rms difference between the computed and least-squares-fitted values of k_4/k_3 is 0.045, revealing that the polynomial fitting is an excellent parameterization to relate k_4/k_3 and the mean effective size (Ou et al. 1993). Thus, it is not necessary

to study the sensitivity of errors in the parameterization of k_4/k_3 on the retrieval.

4. Application to satellite data

For the purpose of testing the removal–retrieval scheme, we have acquired the AVHRR global area coverage (GAC) data collected by *NOAA-9* at about 2100 UTC 28 October 1986. This dataset, including the FIRE IFO region (42°–47°N, 87°–92°W), covers the midwestern United States. It contains the scaled values of latitude, longitude, solar zenith angle, the zenith-normalized channels 1 and 2 radiances, and the brightness temperatures of channels 3, 4, and 5 for each GAC pixel. There are a total of 2.6×10^5 pixels. A program has been developed to unpack the dataset using the calibration procedures documented by Kidwell (1991) to obtain the true data values. We have also developed a program to compute the satellite zenith angle and the relative azimuthal angle based on the viewing geometry of the polar-orbiting satellite. The thermal infrared channels (3, 4, and 5) are constantly calibrated by blackbody calibrators on board the satellite. However, there are no in-flight calibration facilities to monitor the long-term stability of visible channels (1 and 2). Staylor (1990) has estimated that the rate of degradation for these visible channels is about 6% per year. We have accounted for these effects in the calibration procedures.

Using the foregoing data, we have performed retrievals of cirrus cloud parameters over three areas with different scales, as shown in Fig. 8. We first apply the removal–retrieval scheme to a 1° × 1° area over western Wisconsin (the innermost frame in Fig. 8). We then expand the domain of retrievals to a 5° × 5° area associated with the FIRE IFO region (the intermediate frame in Fig. 8). These retrievals are designed for developing and testing an automated removal–retrieval scheme, for verifying the retrieval results against local lidar measurements, and for comparing the retrieval results with those determined from different satellite datasets and retrieval methodologies. The third retrieval domain is the 20° × 30° area over the midwestern United States. These retrievals enable us to test the removal–retrieval scheme over a large area with different satellite viewing geometries and surface characteristics. We also compare our retrieval results with the AVHRR visible cloud picture for the same time period and area.

a. Retrievals over a 1° × 1° area

We have tested the removal–retrieval scheme over a small area (1° × 1°) west of Fort McCoy. Results of this test are presented in the following. The selected zone extends from 43.5° to 44.5°N and from 91° to 92°W. Within this area there are 392 GAC pixels. Figures 9a–c show the halftone display of the channel 1
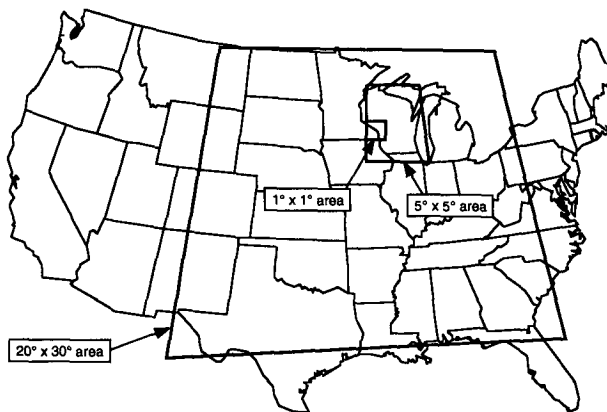

FIG. 8. Three different domains for daytime retrievals over the United States. The smallest domain is a 1° × 1° zone over western Wisconsin. The intermediate domain is a 5° × 5° area over Wisconsin. The largest domain is a 20° × 30° region covering the midwestern United States.

reflectances and the channel 3 and channel 4 brightness temperatures. The darker areas in each frame correspond to lower reflectances or higher brightness temperatures and are associated with either clear or very thin cirrus clouds. The whiter areas correspond to higher reflectances or lower brightness temperatures and are associated with thicker cirrus clouds. The area is mostly covered with clouds during the day. Small clear areas are evident over the eastern and southwestern regions. High reflectances and low brightness temperatures preside over the south-central region. Brightness temperatures are distributed more evenly over the northern half of the area than those over the southern half. This suggests that at the time of satellite overpass, the air mass over the southern half was more dynamically active than the northern half. The clear detection scheme is applied to the satellite data covering the aforementioned area. Figure 10 shows the distribution of clear and cloudy pixels. There are 46 detected clear pixels that are scattered over the eastern and southwestern regions. The clear areas shown in Figs. 9a and 9b are correctly identified in Fig. 10.

To remove the 3.7-μm solar component, we must first determine r_{a1} and r_{a3}. The channel 1 effective surface albedo ($\sim$0.12) is taken to be the mode value of r_1 for all the identified clear pixels. The determination of r_{a3} is somewhat more involved. As described earlier, the surface albedo r_{s3} is fixed at 0.1. However, to determine r_{a3} from Eq. (6), the value of T_3 is required. Two sets of sounding data over the region at 2100 UTC are used in the T_3 calculations. One set is the Green Bay sounding presented by Starr and Wylie (1990), while the other is derived from the ISCCP-C1 sounding profiles (Rossow and Schiffer 1991). The ISCCP sounding profiles are the averages of satellite-derived sounding profiles over a 2.5° × 2.5° area at nine vertical levels. Generally, the temperatures of these two profiles
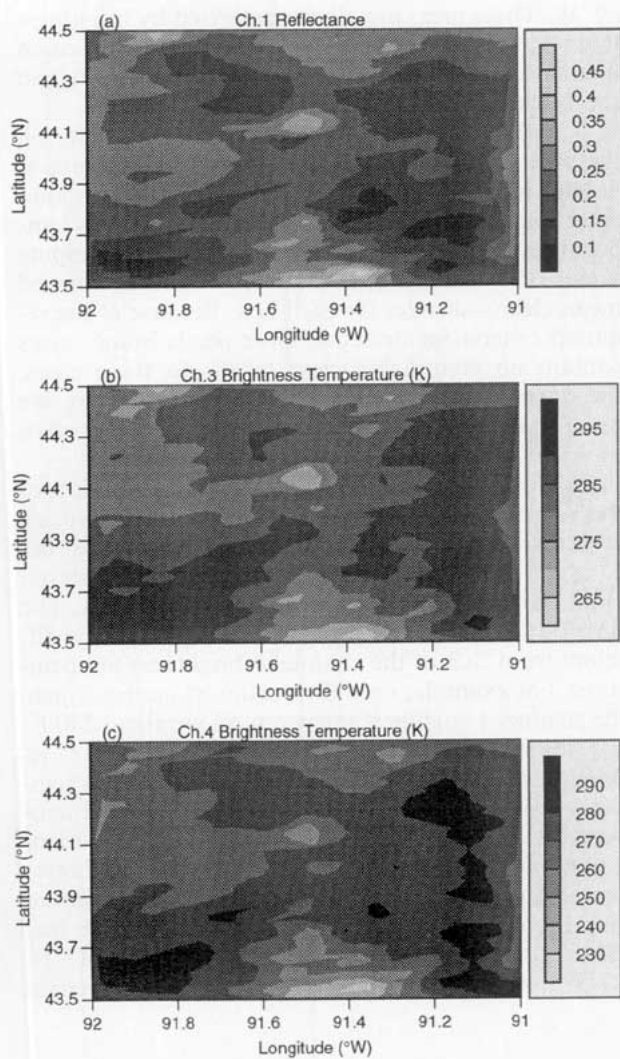
FIG. 9. Halftone display of (a) the channel 1 reflectance, (b) the channel 3 brightness temperature, and (c) the channel 4 brightness temperature for the 1° × 1° area (43.5°–44.5°N, 91°–92°W) over Wisconsin at 2100 UTC 28 October 1986.

detected from the retrieved cloud temperature. Figures 11a–c show the halftone displays of the retrieved T_c, D_e, and τ over the 1° × 1° area, respectively. The distribution of T_c over the northwestern region is relatively homogeneous with values between 230 and 240 K. Sharp transition regions are evident near cold cirrus clouds ($T_c < 225$ K). These features result from the presence of cold cirrus within a clear region. The cold cirrus clouds appear to be associated with cirrus generation regions (Heymsfield 1975). These clouds are relatively high and thin and contain small ice crystals (see Figs. 11b and 11c).

From the distribution of cirrus cloud temperature, we may also qualitatively infer the dynamic activity of the air mass. To the north and east of the sharp transition regions, the distribution of cirrus cloud temperatures is less variant. A transition is seen from the cirrus-growing regions, located at the southwestern side of the cloudy area, to the cirrus-dissipating regions, located at the northeastern side. Considering that the prevalent wind is from the west-southwest direction (Starr and Wylie 1990), this transition pattern may be explained by the theory of cirrus formation and dissipation proposed by Heymsfield (1975). The stable regions over the northern part show that the cirrus clouds there are dissipating. We conclude that the cirrus-growing regions on the southwestern side are dynamically active with vertical motions enhanced by latent heat release, whereas the cirrus-dissipating regions on the northeastern side are dynamically stable. It is likely that within a small area on the order of 100 km × 100 km, newly formed cirrus coexists with mature and dissipating cirrus.

In Fig. 11b, the distribution of D_e corresponds to the distribution of T_c. Sharp transition regions occur over the southern and eastern parts of the area. Over the northern part, the distribution of D_e is relatively uniform; the distribution of τ, shown in Fig. 11c, is also relatively uniform ($\tau = 0$–2.5), except near the south-central part where τ reaches a value greater than

differ by less than 10 K, while the humidities differ by less than 2 g kg^{-1} above 700 mb. The transmittance profiles for the 3.7-μm wavelength are computed using the two sets of soundings. The total transmittance in both cases is about 0.99 because of the low humidity content, implying that the simulated channel 3 transmittance is relatively insensitive to the uncertainty in sounding profiles.

We apply the removal–retrieval scheme to each cloudy pixel that has been identified. As investigated in Ou et al. (1993), the cirrus cloudy condition can be found as the brightness temperature difference between channel 3 (nighttime) and channel 4 larger than 2 K. The channel 3 daytime data, which is contaminated by the solar reflection, cannot be used to identify the presence of cirrus. However, cirrus pixels can be
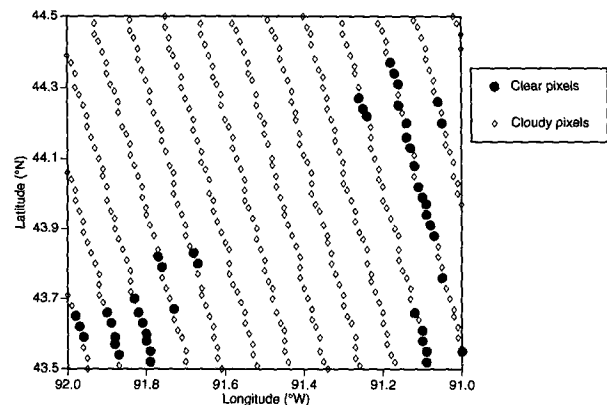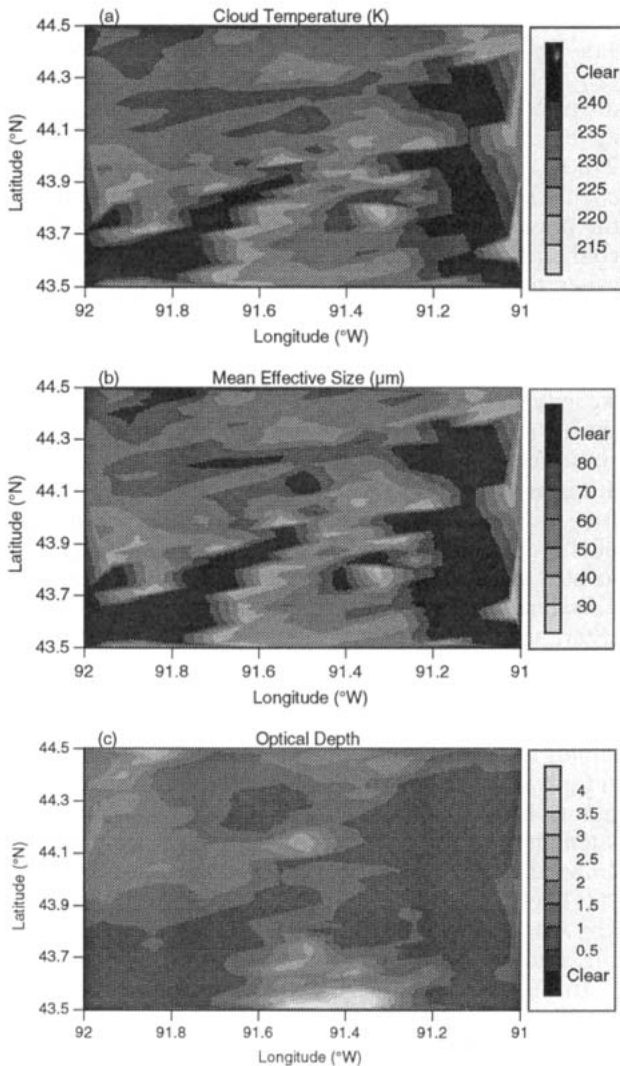

FIG. 10. Distribution of the clear and cloudy pixels that are identified over the 1° × 1° area west of Fort McCoy.

(b) the retrieved mean effective size, and (c) the retrieved optical depth over the $1° \times 1°$ area west of Fort McCoy at 2100 UTC 28 October 1986.

5. It is noted that the distribution of τ does not necessarily match the distribution of T_c. Most of the cold cirrus and warm cirrus regions show relatively small values of τ (0–1.5). Thick cirrus clouds occurring over the south-central part represent a region with high ice water path.

b. Retrievals over a $5° \times 5°$ area

We have also applied the removal–retrieval scheme to the AVHRR daytime data, collected on 28 October 1986 at 2100 UTC over Wisconsin ($42°–47°N$, $87°–92°W$) during the FIRE IFO. The brightness temperature of channel 4 over this area is shown in Fig. 12. The majority of the cloudy areas is located near the northwest corner, at about $44°N$, $91°W$ and $45°N$,

$89°W$. These areas are all characterized by brightness temperatures lower than 260 K. Clear areas are located mainly at $45°N$, $90°W$ and near the northeast and southeast corners.

To reduce the effects of surface inhomogeneity on the mean clear radiances, the whole $5° \times 5°$ area is divided into 25 $1° \times 1°$ boxes to which the clear–cloud detection scheme is applied. Using the brightness temperatures of clear pixels that are identified, we compute a pair of channel 3 and channel 4 thermal infrared mean clear radiances for each box. Because of the required criteria for detecting clear pixels, some boxes contain no identifiable clear pixels. In these cases, the mean clear radiances of a neighboring box are used. The removal–retrieval scheme is then applied to each box.

Figures 13a–d show the geographic distribution of the retrieved cloud temperature, mean effective ice crystal size, optical depth, and cloud height over the $5° \times 5°$ area, respectively. In Fig. 13a, the retrieved cloud temperatures range between 215 and 240 K. The distribution of the retrieved cloud temperature is different from that of the channel 4 brightness temperatures. For example, near the northwest corner, where the channel 4 brightness temperatures are about 240 K, the minimum cloud temperature is about 225 K. Around $45°N$, $89°W$, the channel 4 brightness temperatures are also about 240 K, while the cloud temperatures are about 235 K. However, one degree longitude east of this cloudy area, the channel 4 brightness temperatures are about 255 K, while the minimum cloud temperature is about 220 K. It is possible that cirrus clouds are on top of low clouds near $45°N$, $89°W$. However, a single layer of high, thin cirrus
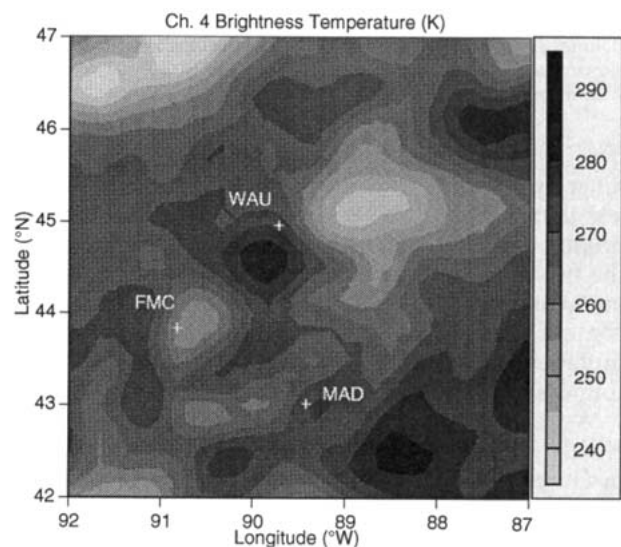

FIG. 12. Halftone display of the channel 4 brightness temperature for the $5° \times 5°$ area over Wisconsin at 2100 UTC 28 October 1986. The crosses identify the location of three FIRE IFO stations.
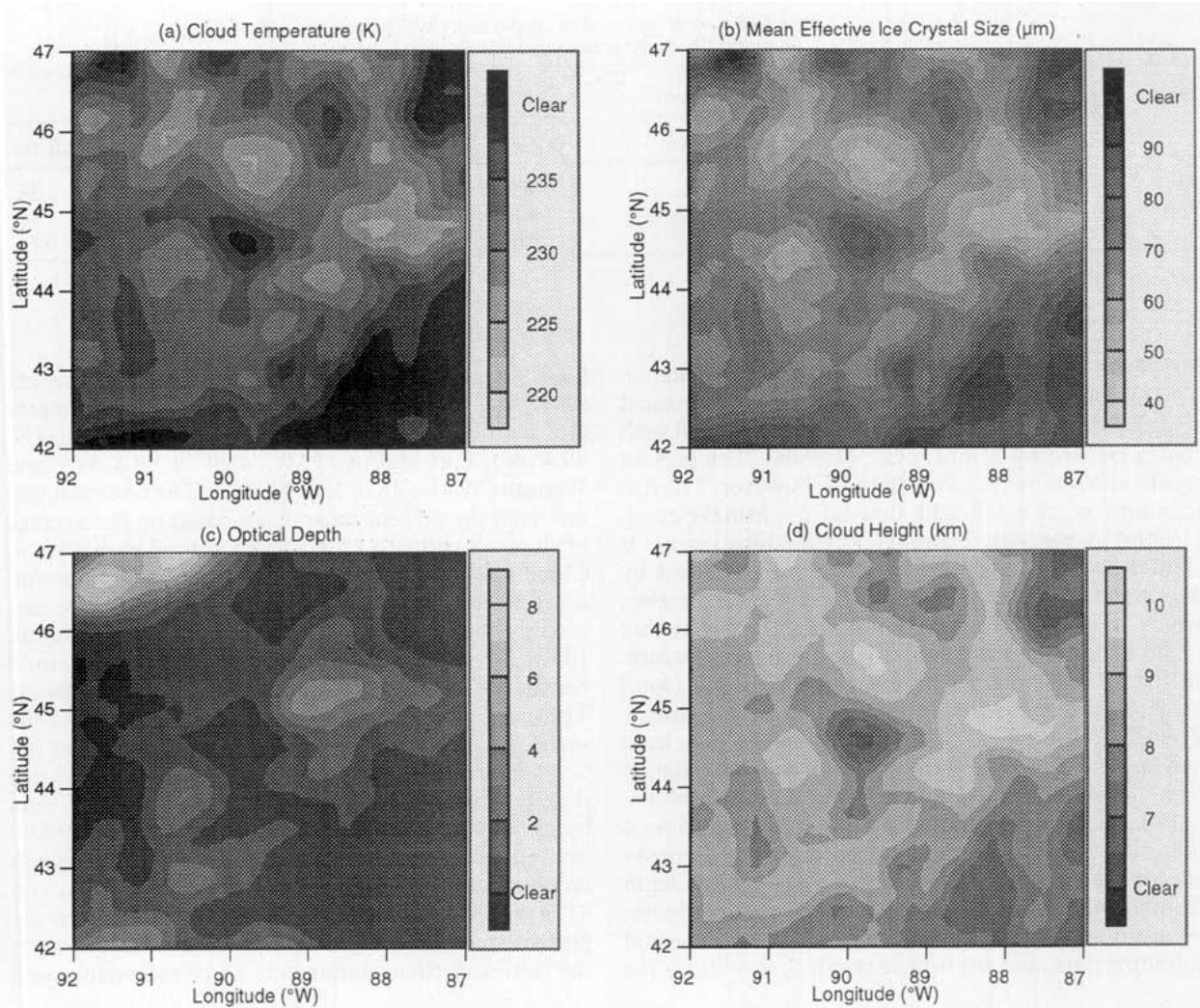
FIG. 13. Halftone display of (a) the retrieved cloud temperature, (b) the retrieved mean effective size, (c) the retrieved optical depth, and (d) the retrieved cloud height over the 5° × 5° area over Wisconsin at 2100 UTC 28 October 1986.

clouds is present near 45°N, 88°W. Over the region where multilayered clouds are present, retrievals had been performed as though there were only a single layer of cloud. This is because reliable methods are yet to be developed for detecting multilayer cloudy pixels using AVHRR data. In Fig. 13b, the distribution of the retrieved mean effective ice crystal sizes, which range between 40 and 100 μm, are in agreement with that of the cloud temperature shown in Fig. 13a. The computed mean effective sizes, however, have not been validated against aircraft observations, because the aircraft data that are properly collocated and coincident with the satellite overpass were not available. In Fig. 13c, the retrieved optical depth ranges between 0 and 8. The map of the optical depth matches that of the channel 4 brightness temperature shown in Fig. 12. In Fig. 13d, the distribution of cloud heights is determined from the distribution of cloud temperature using the averages of the 2100 UTC soundings data at Plattville

and Green Bay, Wisconsin (Starr and Wylie 1990). The cloud heights range between 6 and 11 km. The distribution of cloud height agrees with that of cloud temperature (Fig. 13a) and mean effective ice crystal size (Fig. 13b).

The preceding results are compared with results presented by Minnis et al. (1990b), who also derived the distributions of cloud height and cloud optical depth, using both the AVHRR visible and IR channel data over the same area and for the same time period. Minnis et al. (1990b) derived the optical depth directly from the channel 1 bidirectional reflectances based on radiative transfer calculations (Takano and Liou 1989b). The present removal–retrieval scheme, however, derives the optical depth based on the parameterization of the channel 4 emissivity. Minnis et al. (1990b) showed that the optical depth ranges between 0 and 5 for most of the area. Over the major cloudy areas near the northwest corner and at about 45°N,

TABLE 4. Cirrus cloud temperature, mean effective ice crystal size, cloud height, and optical depth determined from the present retrieval program.

| | T_c (K) | | D_e (μm) | z (km) | | τ | |
	Present	Lidar*	Present	Present	Lidar*	Present	GOES*
WAU	226.5	230.7	57.1	9.5	9.0	1.54	1.43
FMC	229.7	226.5	61.3	9.1	9.5	1.50	1.41
MAD	225.6	228.1	53.9	9.6	9.3	0.60	0.56

* After Minnis et al. (1990a).

89°W, the optical depth is shown to be greater than 5. The distribution of the optical depth from the present removal–retrieval scheme agrees reasonably well with that presented by Minnis et al. (1990b). The present results show more detailed features, however. The distribution of cloud height derived by Minnis et al. (1990b) is between 7 and 11 km for most areas. It should be noted that the cloud heights presented by Minnis et al. (1990b) are the cloud-center heights, which were derived through empirical formulas that relate cloud temperature and cloud-top temperature. In the present scheme, however, the retrieved cloud height is close to the cloud-top height for thicker clouds. Therefore, over most of the cloudy areas, the cloud heights determined from the present scheme are slightly higher than those presented by Minnis et al. (1990b).

Finally, for verifications and comparisons, Table 4 lists the retrieved values of cloud temperature, mean effective ice crystal size, cloud height, and optical depth from the present scheme. Also listed are the cloud temperature and midcloud height derived from lidar and sounding data, and the optical depth derived from the

GOES data (Minnis et al. 1990a). Comparisons are made near the three FIRE IFO stations whose locations are identified in Fig. 12: Madison (MAD; 43.1°N, 89.4°W), Fort McCoy (FMC; 43.9°N, 90.8°W), and Wausau (WAU; 45.0°N, 89.7°W). The retrieved values from the present scheme are based on the average of all pixels within a 1° × 1° area around each station. Cloud temperatures and cloud heights at all three stations determined from the present scheme agree reasonably well with those from lidar data (Sassen et al. 1990). The differences in cloud temperature and cloud height are less than 4.2 K and 0.5 km, respectively. These differences may be caused by the effect of the vertical inhomogeneity within cirrus clouds. The optical depths inferred from the present scheme are slightly larger than those derived from the GOES data by about 0.1. It is noted that Minnis et al. (1990a) derived their optical depths based on a cirrostratus microphysical model with a mean effective size of about 41.5 μm. The mean effective size retrieved from the present study is between 50 and 60 μm. In summary, the retrieved cloud parameters agree reasonably well
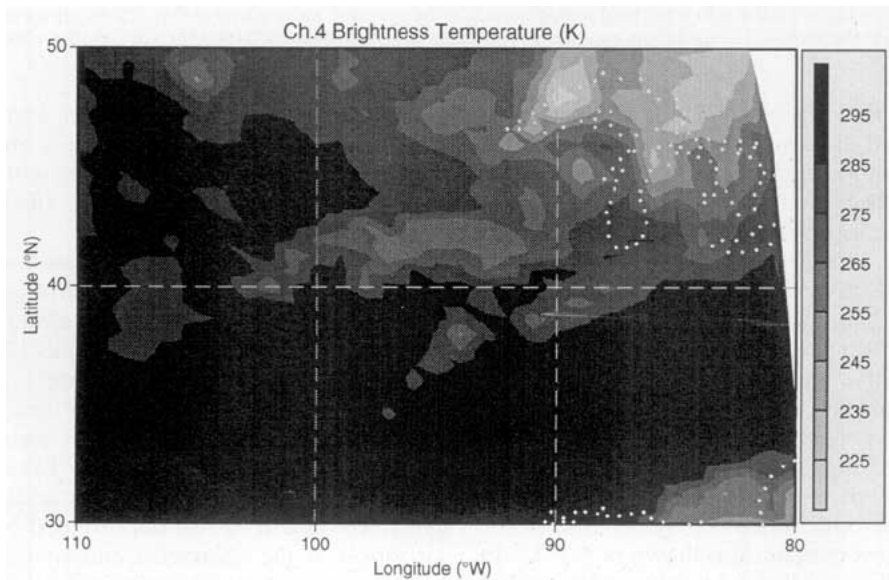

FIG. 14. Display of the channel 4 brightness temperatures over the midwestern United States at 2100 UTC 28 October 1986.

FIG. 15. The AVHRR channel 1 satellite imagery over the midwestern United States at 2100 UTC 28 October 1986.

with the observations and with results computed from different techniques.

c. Retrievals over a 20° × 30° area

We have performed the daytime retrieval of cirrus cloud parameters covering the midwestern United States for 2100 UTC 28 October 1986. Figure 14 shows the display of channel 4 brightness temperatures. The area covered is from 30° to 50°N and from 80° to 110°W. It is evident that clouds are present over the Great Lakes region (outlined by dots over the northeast corner) and the southeast United States. The rest of the area is relatively clear. For comparison, Fig. 15 displays the AVHRR channel 1 satellite imagery based on high-resolution pixel transmission data over the same area and time period.

The data domain is divided into 70 3° × 3° boxes. For each box, we compute a single set of average sun–satellite geometrical parameters for the purpose of correlating channels 1 and 3 reflectances based on radiative transfer calculations. The variations in the solar zenith angle, satellite zenith angle, and relative azimuthal angle for pixels within each box are less than 3°, 8°, and 2°, respectively. Radiative transfer calculations show that these angular variations produce negligible variations in the channels 1 and 3 reflectances. Each box is further divided into nine 1° × 1° miniboxes. The clear–cloud detection program is applied to all pixels in each minibox to obtain the channel 1 effective surface albedo from the mode of the histogram of all channel 1 clear reflectances in the box. We then apply the removal–retrieval scheme to cloudy pixels in each minibox, using a pair of channels 3 and 4 thermal in-

frared clear radiances for each minibox. If no clear pixels are detected within the minibox, the clear radiances of a neighboring box are used. The averages of Green Bay and Plattville soundings at 2100 UTC are employed to compute the transmittances for clear atmospheres.

Figures 16a–c display the retrieved cirrus cloud temperatures, optical depths, and mean effective sizes, respectively. Over the northern Great Lakes region, cloud temperatures are lower ($\sim$230 K), with larger pockets of cold cirrus ($<$230 K) than over the southeastern corner. Moreover, the corresponding cloud optical depths are larger than 8 over the Great Lakes region. Small mean effective sizes ($<$50 μm) are found near the northern edge of Lake Superior. These retrieval results are consistent with the high-resolution satellite cloud picture shown in Fig. 15. To the northeast and east of the Great Lakes, the area is mostly covered with clouds. The visible satellite cloud picture indicates that the same area is relatively dark, due probably to the large solar zenith angle over that area ($\sim$80°). Moreover, the channel 4 brightness temperatures are less than 245 K and the brightness temperature difference
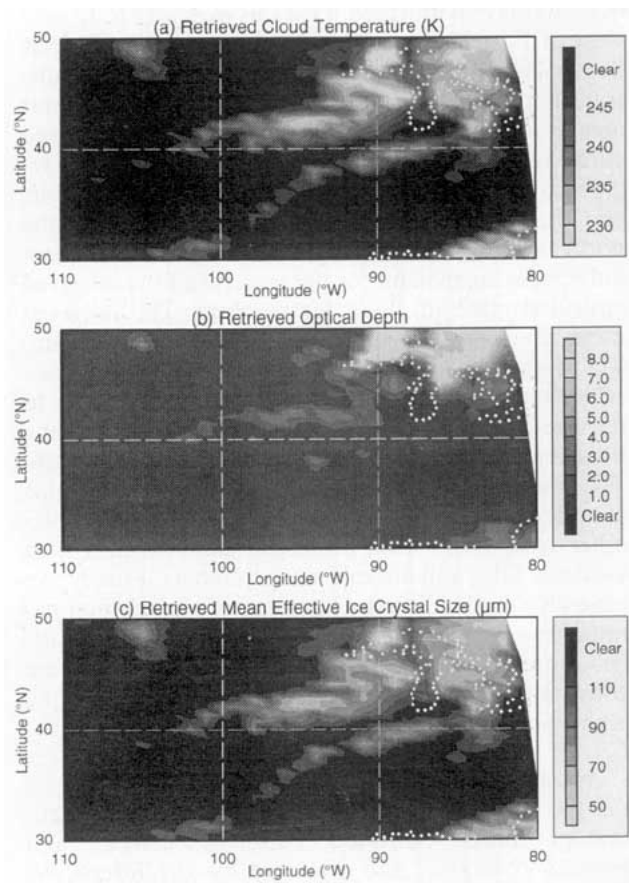

FIG. 16. Display of (a) the retrieved cloud temperature, (b) the retrieved optical depth, and (c) the retrieved mean effective sizes over the area shown in Fig. 8.

between channels 4 and 5 are between 2 and 3 K, indicating the presence of thick cirrus over that region. Although it is possible that low-level clouds could have been present, reliable schemes for detecting multilayer cloud systems are yet to be developed to identify this situation.

5. Conclusions

A removal–retrieval technique based on radiative transfer parameterizations has been developed for inferring cirrus cloud parameters during local daytime. This scheme uses radiance data of AVHRR 3.7- and 10.9-μm channels to simultaneously determine cirrus temperature, mean effective ice crystal size, and optical depth. During the local daytime, the 3.7-μm (channel 3) solar component is removed by using the correlation between channel 1 (0.63 μm) and channel 3 solar reflectances. This correlation is derived from radiative transfer calculations.

We have carried out sensitivity studies on the accuracy of the removal scheme. Overall, for optical depths larger than 1, the maximum percentage error in the 3.7-μm solar component is less than 10%. Moreover, we have performed retrievals over a $1° \times 1°$ area west of Fort McCoy, Wisconsin, using the AVHRR data collected at 2100 UTC 28 October 1986. The distribution of channel 4 brightness temperature over this area shows distinct clear regions. Based on the retrieved cloud temperature, several cold cirrus-generating regions are shown along with large areas of warm, stable, and dissipating cirrus clouds that are present to the north and east of the cirrus-forming regions. Significant differences are evident for the patterns of the retrieved optical depth and cloud temperature. The retrieved mean effective ice crystal sizes range from 30 to 90 μm, which appear to be consistent with the observed values.

We have applied the removal–retrieval scheme to retrieve cirrus parameters over a $5° \times 5°$ area, using the same daytime dataset collected on 28 October 1986. The retrieved cloud temperatures and cloud heights compare reasonably well with the results presented by other researchers using different methods and with available lidar and aircraft measurements. Finally, we have also carried out the mapping of cirrus cloud parameters over the midwestern United States. The distributions of the retrieved cirrus cloud parameters are consistent with the satellite cloud picture based on the high-resolution AVHRR channel 1 reflectances.

REFERENCES

Air Force Geophysics Laboratory, 1985: *Handbook of Geophysics and the Space Environment*, 80 pp.
Allen, R. C., P. A. Durkee, and C. H. Wash, 1990: Snow/cloud discrimination with multispectral satellite measurements. *J. Appl. Sci.*, **29**, 994–1004.
Arking, A., and J. D. Childs, 1985: Retrieval of cloud cover parameters from multispectral satellite images. *J. Climate Appl. Meteor.*, **23**, 322–333.
Auer, A. H., and D. L. Veal, 1970: The dimension of ice crystals in natural clouds. *J. Atmos. Sci.*, **27**, 919–926.
Bunting, J. T., and K. R. Hardy, 1974: Cloud identification and characterization from satellites. *Satellite Sensing of a Cloudy Atmosphere: Observing the Third Planet*, A. Henderson-Sellers, Ed., Taylor and Francis, 203–240.
Chou, M. D., 1991: The derivation of cloud parameters from satellite-measured radiances for use in surface radiation calculations. *J. Atmos. Sci.*, **48**, 1549–1559.
Dudhia, A., 1989: Noise characteristics of the AVHRR infrared channels. *Int. J. Remote Sens.*, **10**, 637–644.
Heymsfield, A. J., 1975: Cirrus uncinus generating cells and the evolution of cirriform clouds. Part I: Aircraft observations of the growth of the ice phase. *J. Atmos. Sci.*, **32**, 799–808.
——, and C. M. R. Platt, 1984: A parameterization of the particle size spectrum of ice clouds in terms of the ambient temperature and the ice water content. *J. Atmos. Sci.*, **41**, 846–855.
——, K. M. Miller, and J. D. Spinhirne, 1990: The 27–28 October 1986 FIRE IFO cirrus case study: Cloud microstructure. *Mon. Wea. Rev.*, **118**, 2313–2328.
Kidwell, K. B., 1991: *NOAA Polar Orbiter Data Users Guide.* NOAA/NESDIS, 280 pp.
Kleespies, T. J., 1993: Retrieval of cloud parameters by multiple observations in the near-infrared under conditions of varying solar illumination. *Proc. SPIE OE/Aerospace and Remote Sensing Symposium*, Orlando, FL, SPIE, 338–345.
Liou, K. N., 1980: *An Introduction to Atmospheric Radiation.* Academic Press, 392 pp.
——, 1986: Influence of cirrus clouds on weather and climate processes: A global perspective. *Mon. Wea. Rev.*, **114**, 1167–1199.
——, 1992: *Radiation and Cloud Processes in the Atmosphere.* Oxford University Press, 487 pp.
——, S. C. Ou, Y. Takano, F. P. J. Valero, and T. P. Ackerman, 1990: Remote sounding of the tropical cirrus cloud temperature and optical depth using 6.5 and 10.5 μm radiometers during STEP. *J. Appl. Meteor.*, **29**, 716–726.
Minnis, P., D. F. Young, K. Sassen, J. M. Alvarez, and C. J. Grund, 1990a: The 27–28 October 1986 FIRE IFO cirrus case study: Cirrus parameter relationships derived from satellite and lidar data. *Mon. Wea. Rev.*, **118**, 2402–2425.
——, P. W. Heck, and E. F. Harrison, 1990b: The 27–28 October 1986 FIRE IFO cirrus case study: Cloud parameter fields derived from satellite data. *Mon. Wea. Rev.*, **118**, 2426–2446.
——, K. N. Liou, and Y. Takano, 1993a: Inference of cirrus cloud properties using satellite-observed visible and infrared radiances. Part I: Parameterization of radiance fields. *J. Atmos. Sci.*, **50**, 1279–1304.
——, P. W. Heck, and D. F. Young, 1993b: Inference of cirrus cloud properties from satellite-observed visible and infrared radiances. Part II: Verification of theoretical cirrus radiative properties. *J. Atmos. Sci.*, **50**, 1305–1322.
Ou, S. C., K. N. Liou, W. M. Gooch, and Y. Takano, 1993: Remote sensing of cirrus cloud parameters using advanced very-high-resolution radiometer 3.7- and 10.9-μm channels. *Appl. Opt.*, **32**, 2171–2180.
Rossow, W. B., and R. A. Schiffer, 1991: ISCCP cloud data products. *Bull. Amer. Meteor. Soc.*, **72**, 2–20.
Sassen, K., C. J. Grund, J. D. Spinhirne, M. M. Hardesty, and J. M. Alvarez, 1990: The 27–28 October 1986 FIRE IFO cirrus case study: A five lidar overview of cloud structure and evolution. *Mon. Wea. Rev.*, **118**, 2288–2311.

Saunders, R. W., and K. T. Kriebel, 1988: An improved method for detecting clear sky and cloudy radiances from AVHRR data. *Int. J. Remote Sens.*, **9**, 123–150.

Starr, D. O. C., and D. P. Wylie, 1990: The 27–28 October 1986 FIRE cirrus case study: Meteorology and clouds. *Mon. Wea. Rev.*, **118**, 2259–2287.

Staylor, W. F., 1990: Degradation rates of the AVHRR visible channel for the NOAA 6, 7, and 9 spacecraft. *J. Atmos. Oceanic Technol.*, **7**, 411–423.

Sutherland, R. A., 1986: Broadband and spectral emissivities (2–18 μm) of some natural soils and vegetation. *J. Atmos. Oceanic Technol.*, **3**, 199–202.

Takano, Y., and K. N. Liou, 1989a: Solar radiative transfer in cirrus clouds. Part I: Single-scattering and optical properties of hexagonal ice crystals. *J. Atmos. Sci.*, **46**, 3–19.

——, and ——, 1989b: Solar radiative transfer in cirrus clouds. Part II: Theory and computation of multiple scattering in an anisotropic medium. *J. Atmos. Sci.*, **46**, 20–36.

Thekaekara, M. P., 1974: Extraterrestrial solar spectrum, 300–6100 Å at 1 Å intervals. *Appl. Opt.*, **13**, 518–522.

Weinreb, M. P., and M. L. Hill, 1980: Calculation of atmospheric radiances and brightness temperatures in infrared window channels of satellite radiometers. NOAA Tech. Rep. NESS 80, 40 pp.

Wielicki, B. A., J. T. Suttles, A. J. Heymsfield, R. M. Welch, J. D. Spinhirne, M.-L. C. Wu, D. O'C. Starr, L. Parker, and R. F. Arduini, 1990: The 27–28 October 1986 FIRE IFO cirrus case study: Comparison of radiative transfer theory with observations by satellite and aircraft. *Mon. Wea. Rev.*, **118**, 2356–2376.